Short Communication

Formation of metastable bcc-δ phase and its transformation to fcc-γ in laser powder bed fusion of Fe−Mn−Si shape memory alloy

Dohyung Kim [a,b], *Irene Ferretto* [c], *Jong Bae Jeon* [d], *Christian Leinenbach* [c,**], *Wookjin Lee* [a,b,*]

[a] *Dongnam Division, Korea Institute of Industrial Technology, Yangsan, 50623, Republic of Korea*
[b] *Department of Materials Science and Engineering, Pusan National University, Busan, 46241, Republic of Korea*
[c] *Empa − Swiss Federal Laboratories for Materials Science and Technology, Überlandstrasse 129, CH-8600, Dübendorf, Switzerland*
[d] *Department of Materials Science and Engineering, Dong-A University, Busan, 49315, Republic of Korea*

ARTICLE INFO

ABSTRACT

The phase transformation behavior from metastable bcc-δ to fcc-γ in Fe−Mn−Si based shape memory alloy processed by laser powder bed fusion was investigated. Primary δ phase formed in this alloy due to the rapid cooling and fast solidification. Bcc-δ to fcc-γ phase transformation occurred when the volumetric energy density was high due to the process-inherent heat treatment effect. Transmission electron microscope studies confirmed Kurdjumov-Sachs orientation relationship between bcc-δ and fcc-γ phases. The analytical results revealed that the phase transformation occurred by a combined displacive-diffusional mechanisms.

1. Introduction

Laser powder bed fusion (L-PBF) is an additive manufacturing technique that allows printing three-dimensional metallic objects assigned by computer-aided design models through a layer-by-layer process. For the past decade, researchers have discovered that the L-PBF under optimized process could provide excellent mechanical properties which are sometimes even better than those of the same alloy produced by conventional methods such as casting or hot working [1]. During the L-PBF process, a focused laser beam introduces localized melting of powdered metal and eventually leads to extremely high cooling rates up to 10^5−10^6 °C/s [2]. As a result, L-PBF offers fine and unique microstructures which are responsible for the excellent mechanical properties.

Fe−Mn−Si based alloys have been extensively studied in the literature due to their ability of having shape memory effect (SME) [3,4]. The SME of these alloys is devoted to the reversible phase transformations between parent γ-austenite

---

* Corresponding author.
** Corresponding author.
E-mail addresses: christian.leinenbach@empa.ch (C. Leinenbach), wkjinlee@kitech.re.kr (W. Lee).

and strain-induced hcp-ε martensite (hexagonal close packed). The γ to ε and its reverse phase transformation in this alloy system are accomplished by the movement of Shockley-type partial dislocations. The SME of the Fe–Mn–Si based alloys has been extensively studied in the literature, usually by using the alloys produced by conventional metallurgical methods such as hot rolling [5]. It has been known that the SME of the Fe–Mn–Si alloy can be significantly improved by increasing the Shockley-type stacking fault density of the parent γ-austenite phase. For instance, Nishimura et al. [6] investigated the effect of a thermomechanical training treatment by cyclic deformation and heating on the SME of a single crystal Fe–31Mn–6Si (wt.%) alloy. They showed that the training treatment leads to a pronounced increase of the SME by introducing stacking faults. Rong et al. [7] studied the SME of hot rolled Fe–30Mn–6Si (wt.%) alloy. They found that aus-forming of the alloy can significantly improve the SME of the alloy due to the increased stacking fault density. Later, it has been reported that the SME of the Fe–Mn–Si alloy can be enhanced without training treatment but by simply precipitating fine carbides such as NbC and VC, e.g. as shown by Kajiwara et al. [8] and Dong et al. [9]. These studies indicated that the fine and hard precipitates can also introduce high densities of stacking faults which increase the SME of the alloys. More recently, the alloy Fe–17Mn–5Si–10Cr–4Ni (wt.%) was shown to exhibit good combination of strength, toughness and SME [10].

A recent study done by the present authors reported that a fully functional Fe–17Mn–5Si–10Cr–4Ni shape memory alloy with complex 3D shapes can be fabricated by L-PBF [11]. The study reported the optimal volumetric energy density (VED) for L-PBF, the resulting microstructures, mechanical properties and the higher SME in comparison with conventionally fabricated alloys with similar composition. The study also indicated that bcc-δ ferrite (body centered cubic) is the primary phase upon solidification and that rather large amounts of δ-ferrite are maintained in the fabricated parts when relatively low VEDs are used. The fraction of the fcc-γ phase increased with increasing the VED. Such behavior has not been reported for the Fe–Mn–Si alloys produced with methods other than the L-PBF. For instance, the same alloys processed by conventional hot forging method consisted of near full γ austenite [12,13]. Similar observations, i.e. primary bcc-δ phase formation with by-passing of austenite during solidification, were recently made for AISI 17-4 PH Stainless steel fabricated by L-PBF [14]. However, an important but still open question is how the bcc-δ to fcc-γ phase transformation takes place during L-PBF. A better understanding of the evolution of the microstructure during the phase transformation is needed to design and control the microstructure of the Fe–Mn–Si alloy produced by L-PBF.

In this study, the δ → γ phase transformation from the above-mentioned primary bcc-δ phase in Fe–Mn–Si alloy produced by L-PBF has been investigated in detail through electron backscatter diffraction (EBSD), X-ray diffraction (XRD) and transmission electron microscopy (TEM).

2. Experimental details

Gas atomized spherical Fe–17Mn–5Si–10Cr–4Ni (wt.%) shape memory alloy (Fe-SMA) powder (Metal Player Co., Ltd, Republic of Korea) with an average diameter of ~25 μm, which has been investigated in the previous study [11], was used as the starting material for L-PBF. Cube-shaped specimens with a dimension of $5 \times 5 \times 5$ mm^3 were prepared using an OPM250L L-PBF machine (Sodick Co., Ltd, Japan), equipped with an ytterbium fiber laser with a wavelength of 1070 nm, and a maximum laser output of 500 W (YLR-500-WC, IPG, Laser GmbH, Germany). The laser spot has a Gaussian beam distribution and a size of 200 μm. L-PBF was performed with fixed scanning speed (v), hatch spacing (h) and lamination thickness (t) of 800 m/s, 0.1 mm and 0.05 mm, respectively, using three different laser powers (P) of 380, 400 and 420 W. The VED (E), defined as

$$E = \frac{P}{v \cdot h \cdot t} \qquad (1)$$

are 95, 100 and 105 J/mm^3 for the laser powers of 380, 400 and 420 W, respectively. During L-PBF of each layer, an additional laser contour scanning was conducted with the same laser power along the contour line after the core part of each layer was laser scanned. A bidirectional scan strategy with a 90° rotation between the layers was applied for all samples.

Microstructural characterization of the samples was carried out using optical microscope (OM, Eclipse E200, Nikon, Japan). Samples for the OM analysis were mechanically ground using SiC papers and subsequently polished with diamond and colloidal silica suspensions. Then, the samples were color etched using a 0.5% NH$_4$HF$_2$ and 1.2% K$_2$S$_2$O$_5$ (wt.%) solution in distilled water. This color etching method has been widely used and verified for phase characterization of Fe–Mn–Si alloys [15,16]. Inverse pole figure (IPF) maps and pole figures (PF) were obtained by JEOL JSM7200F scanning electron microscope (SEM) equipped with Oxford Nordlysnano EBSD and PANanalytical Empyrean XRD for texture characterization. Phase maps were also obtained by EBSD analysis. To investigate the crystallographic relationship between bcc-δ and fcc-γ, a TEM analysis was carried out (Thermofisher Titan Themiz Z). The TEM specimen was prepared using a Thermofisher Helios G4 UC focused ion beam machine. The analysis was performed with an acceleration voltage of 300 kV.

3. Results and discussion

Fig. 1 shows the OM microstructures of the samples produced by L-PBF with three different laser powers. BD and SD in the OM images indicate the L-PBF building and laser scanning directions, respectively. In the OM images, the fcc-γ phase appears in light brown and bcc-δ appears in dark grey [13]. At the low laser power of 380 W, the microstructure is mainly composed of bcc-δ grains as shown in Fig. 1(a). The phase fraction of bcc-δ phase in this case was ~94% (estimated using
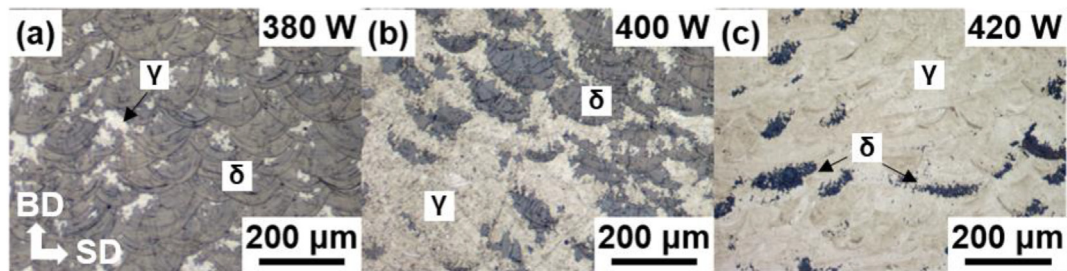
Fig. 1 — OM images of samples produced by L-PBF with different laser powers of (a) 380, (b) 400 and (c) 420 W. The L-PBF building direction is vertical in the OM images.

the Image J software). Bcc-δ has been reported to be the primary solidification phase in high-Mn austenitic steels for which the ratio between the ferrite stabilizing elements given by the chromium equivalent, Cr_{eq}, and the austenite stabilizing elements given by the nickel equivalent, Ni_{eq}, is greater than 1.5 [16]. Upon further cooling, the bcc-δ phase usually transforms into fcc-γ gamma phase at relatively high temperatures at > 1200 °C, depending on the steel's composition. Some of the bcc-δ phase may be retained after fast cooling. In welded or strip casted stainless steel, e.g. AISI 304 or 316 L, the amount of retained bcc-δ phase is typically between 2 and 6% and does scarcely exceed 10% [17,18]. To the best of the authors' knowledge, such abnormally high fractions of bcc-δ as the ones reported here have not been observed for any Fe-based alloy processed with technologies other than L-PBF. A possible reason for this unique bcc-δ microstructure is assumed to be the high cooling rates during L-PBF. As pointed out by Alnajjar et al. [14], the transformation from bcc-δ to fcc-γ is hindered in this case because there is not enough time for the transformation to occur. With increasing laser power, the volume fraction of the fcc-γ phases gradually increases. This result is well in accordance with the previous study [11]. The microstructure of the sample produced with 400 W laser power consists of more fcc-γ and less bcc-δ than sample produced with 380 W with area fractions of approximately 48% and 52%, respectively. The sample produced with 420 W laser power is characterized by a near fully fcc-γ microstructure with a γ fraction of ~93%, as shown in Fig. 1(c). A phase

analysis was also performed using the theta-two theta XRD method (see Supplementary Material). However, the phase fractions derived from the XRD measurements are considered inaccurate because of the strong texture of the samples. Nevertheless, the trend of increasing amount of bcc-δ with decreasing VED could be confirmed.

Fig. 2 shows OM micrographs of the sample produced with 420 W laser power near the top-most layer and contour scanned area. The bcc-δ phase fraction in the top-most layer is clearly much higher than in the other layers, as shown in Fig. 2(a). It implies that, upon rapid solidification, the alloy contained a high volume fraction of bcc-δ, and then a phase transformation from bcc-δ to fcc-γ took place while the next layer was deposited. Fig. 2(b) shows the microstructure near the outer surface of the sample where the additional laser contour scanning was applied during the L-PBF. It shows evidently that the contour scanned area has much less bcc-δ phase fraction than in the core area. The contour scanned area was irradiated twice in every single layer scanning process while the core part was irradiated only once. Considering this, the relatively low bcc-δ fraction in the contour scanned area can be explained by the additional bcc-δ to fcc-γ phase transformation occurring in this area due to the laser contour scanning effect.

The results presented in Fig. 2 indicate that the primary solidification phase of the Fe-SMA in the L-PBF is bcc-δ and the fcc-γ phase forms apparently after a solid state phase transformation during the deposition of the following layers. The
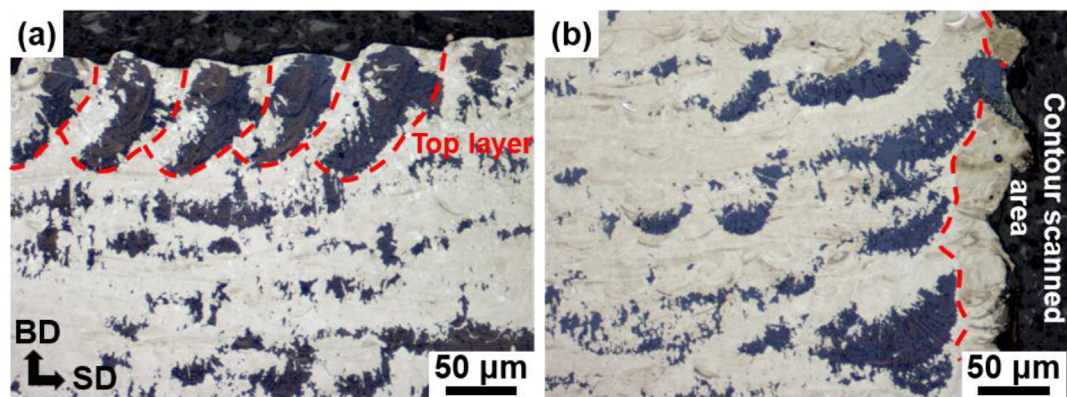

Fig. 2 — OM images of the sample produced with laser power of 420 W. (a) Near top-most layer and (b) near contour scanned area.

mechanism leading to this phase transformation is assumed to be the so-called intrinsic heat treatment (IHT), during which a pre-deposited layer is in the heat-affected zone (HAZ) of the layer above and undergoes cyclic heat treatments during the deposition of the next layers [19,20], with diminishing intensity after each layer. For example, Günther et al. [21] have shown that a pre-deposited steel alloy layer can be easily heated to more than 1200 °C during the deposition of the following layers. It is known from the literature [14,16,17] that retained bcc-δ in austenitic stainless steels transforms into fcc-γ after a heat treatment at temperatures 700−1200 °C. It is hypothesized that with increasing laser power and thus an increasing VED, the more heat will be transferred to the pre-deposited layer. This leads to higher peak temperatures, larger heat affected zones as well as lower cooling rates and thus longer times at elevated temperatures [22,23]. This will result in a more pronounced IHT in the HAZ with a faster and more pronounced transformation from bcc-δ to fcc-γ during the L-PBF process.

Fig. 3(a−f) shows the EBSD inverse pole figures and phase maps of the samples produced with laser powers of 380, 400 and 420 W. The EBSD phase analysis for the laser powers of 380 and 400 W reveals coarse bcc-δ structures with elongated grains along the BD, indicating the formation of bcc-δ phase during the solidification. In contrast, the transformed fcc-γ appears as fine and equiaxed grains in the EBSD maps with the simultaneous appearance of small amounts of hcp-ε phase in them. The overall grain size becomes finer with increasing the L-PBF laser power, i.e. the higher the VED, the higher the amount of fine fcc-γ grains. This behavior is seemingly counter-intuitive because higher VEDs typically lead to coarser grain structures due to a higher heat input into the melt pool and the HAZ, leading to lower solidification velocities. In the present case, the formation of fcc-γ nuclei from bcc-δ is largely suppressed if the cooling rate exceeds a certain threshold value (i.e. at low VEDs), and the bcc-δ grains, epitaxially grown as primary phase during deposition, are maintained at low temperatures after cooling. At high VEDs, the IHT effect is more pronounced and the cooling rate is
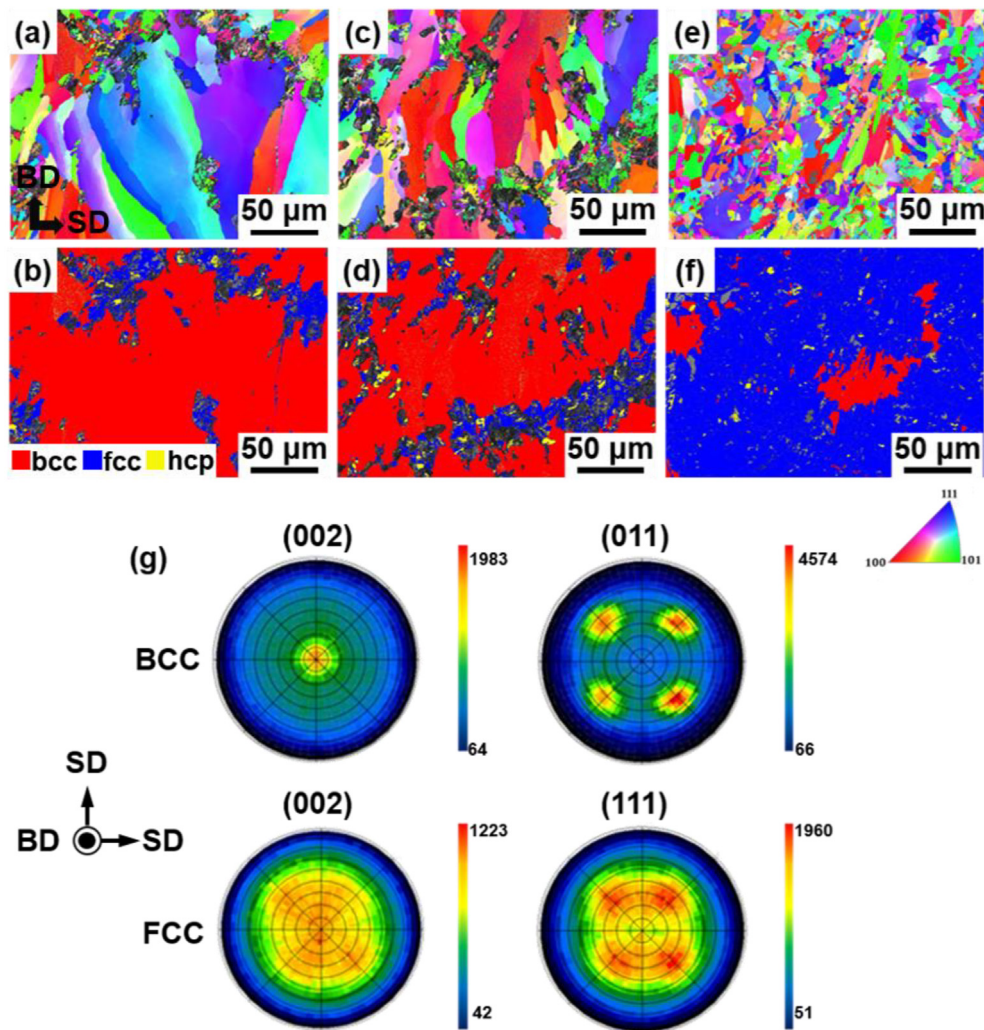

Fig. 3 − (a, c, e) EBSD inverse pole figure maps along L-PBF building direction and (b, d, f) phase maps for samples produced with laser powers of (a, b) 380, (c, d) 400 and (e, f) 420 W. (g) XRD pole figures of sample produced with laser power of 400 W.

sufficiently low. The primary bcc-δ phase can therefore transform into fcc-γ in a solid-state transformation during cooling of the solidified layers. The fcc-γ grains are formed along the grain boundaries of the original bcc-δ grains, as shown in Fig. 3(a–c). The fcc-γ grains can grow entirely across the bcc-δ grains, leading to the almost fully austenitic fine microstructure observed in high-VED samples.

Fig. 3(g) shows the XRD pole figures of the sample produced with a laser power of 400 W. The bcc-δ phase exhibits a strong rotated-cube texture in a way that the {002} plane normal is parallel to the BD and the {011} plane normal is rotated by 45° with regard to the BD from $\{100\}_{BD}<001>_{SD}$ cube orientation. Such a pronounced rotated-cube texture is not surprising since it is often observed when bcc-structured alloy is produced by L-PBF using the bidirectional 90° rotation scan strategy, as reported e.g. in [24]. In the case of transformed fcc-γ grains, the texture $<111>_{SD}$ was less pronounced than in the original bcc-δ grains. The texture components $(110)_δ$ are aligned with those of the $(111)_γ$, revealing a high coherency between the original bcc-δ and the transformed fcc-γ grains with Kurdjumov-Sachs (K–S) or Nishiyama-Wasserman (N–W) orientation relationships [25]. Therefore, the pole figure analysis implies that fcc-γ inherited texture from the strongly textured bcc-δ phase.

The TEM analysis results are illustrated in Fig. 4. Fig. 4 (a) shows fine parallel line contrasts in the fcc-γ grain formed by the shear-induced transformation. Most of these lines are stacking faults between two $\{111\}_γ$ planes, which were presumably introduced by the migration of a strictly oriented coherent interface during the shear-induced bcc-δ to fcc-γ transformation. As pointed out by Kajiwara et al. [26], these stacking faults can promote the stress-induced fcc-γ to hcp-ε transformation and thereby increase the SME. In the case of the Fe-SMA produced by L-PBF, it appears that dense stacking fault arrays are easily obtained by transforming bcc-δ into fcc-γ grains through the IHT during L-PBF. Indeed, the Fe-SMA produced by L-PBF showed a recovery strain of up to 1.65% after 4% pre-straining and heating to 200 °C as reported in the previous study [11], which is significantly higher than the recovery strain of 1.15% achieved with conventionally processed alloy under the same test condition [27]. The thermal residual stress from the rapid solidification and thermal strain mismatch between the bcc-δ and fcc-γ during L-PBF may also promote the formation of the stacking faults.

The selected area electron diffraction pattern in Fig. 4(b), which was taken near the interface between bcc-δ and fcc-γ phases as indicated in Fig. 4(a), shows clearly that the transformed fcc-γ has the Kurdjumov-Sachs (K–S) orientation relationship with respect to the original bcc-δ grain, i.e. $\{111\}_γ//\{011\}_δ$ and $<011>_γ//<111>_δ$. Considering this highly cohesive orientation relationship together with the observation of high stacking fault density in the fcc-γ grains that are presumably formed by the shear-induced transformation, it is assumed that a displacive bcc-to-fcc transformation indicative for a martensitic transformation occurred. Such a behavior is unusual since phase transformations from bcc-δ to fcc-γ generally take place via the peritectic mode with element redistribution or via massive transformation, which is a diffusional process accompanied by large strains but without element redistribution and crystallographic orientation relationship [28]. This might be due to the very localized and rapid heating by the fast scanning laser, i.e. 800 mm/s in this study. In this case, the transformation triggered by the IHT can take place without sufficient time for diffusion so that the recrystallization remains incomplete.

As shown in Fig. 3(a), the nucleation of fcc-γ occurred at the bcc-δ grain boundaries as they can act as preferred nucleation sites. This can explain the gradually increasing fraction of fcc-γ phase with increasing VED. Since the nucleation of fcc-γ can effectively act as the energy barrier, the bcc-δ to fcc-γ transformation will be limited for the low VED. However, the much finer fcc-γ grain structure in comparison with the original bcc-δ grains as well as the weakened fcc-γ texture indicate that the shear-induced displacive transformation is not the only mechanism for the bcc-δ to fcc-γ transformation. Such fine and
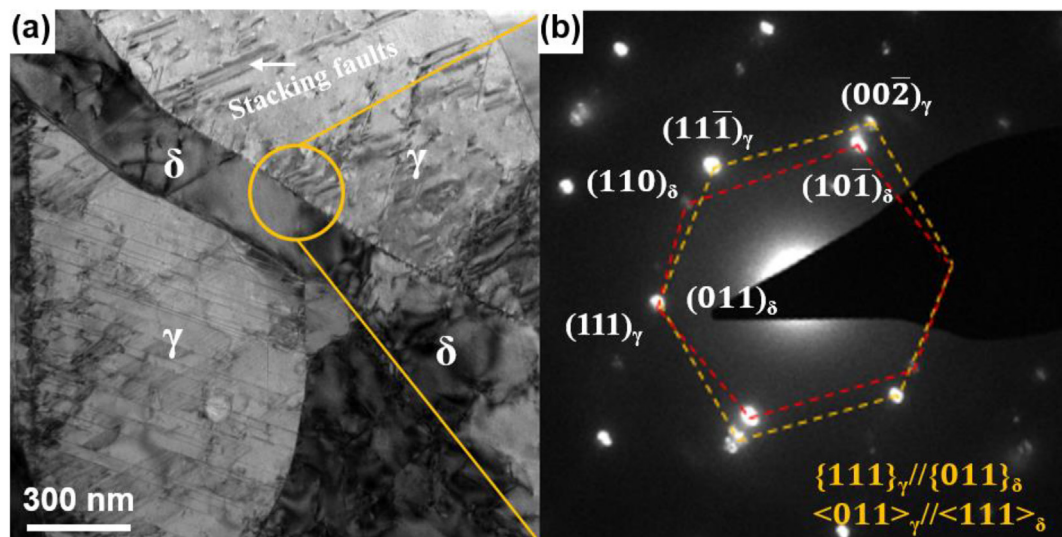

Fig. 4 – **(a) TEM bright field image of sample produced with laser power of 400 W and (b) selected area electron diffraction pattern in the region of yellow circle in (a). The zone axis is $\langle11\bar{1}\rangle_δ//\langle01\bar{1}\rangle_γ$.**

equiaxed fcc-γ grain structures are typically obtained from the formation of recrystallized fcc-γ grains in the reverse martensitic transformation via a diffusive mechanism [29]. As shown in Fig. 4 (a), the fcc-γ grains near the δ/γ interface, which are believed to be transformed by the displacive mechanism, are characterized by high stacking fault densities. Such high stacking fault densities are assumed to provide sufficient driving force for the recrystallization during the cyclic re-heating of the samples. However, the verification of this hypothesis would require sophisticated methods such as in situ TEM or high-energy (synchrotron) XRD during rapid heating and cooling, which is beyond the scope of the present work.

4. Summary and conclusions

In summary, the bcc-δ to fcc-γ phase transformation from the primary bcc-δ phase in a Fe-based shape memory alloy produced by laser powder bed fusion has been investigated. The primary solidification phase of the Fe-based shape memory alloy during laser powder bed fusion was bcc-δ with strong <001> texture along building direction, which was retained in large amounts at room temperature due to the high cooling rates during laser powder bed fusion. When the volumetric energy density during laser powder bed fusion is high, the primary bcc-δ phase was transformed into fine fcc-γ grains due to the intrinsic heat treatment effect and the resulting lower cooling rates in comparison with samples fabricated at lower volumetric energy density. The transmission electron microscopy analysis revealed that the fcc-γ grain adjacent to its original bcc-δ grain strictly follows the Kurdjumov-Sachs orientation relationship. Furthermore, high stacking fault densities are achieved during phase transformation due to high coherency between bcc-δ and fcc-γ. Together with the observation of fine and equiaxed fcc-γ grain structures, the transmission electron microscopy results indicated that the bcc-δ to fcc-γ phase transformation occurred by a combined displacive-diffusional mechanisms.

Declaration of Competing Interest

The authors declare that they have no known competing financial interests or personal relationships that could have appeared to influence the work reported in this paper.

Acknowledgement

Appendix A. Supplementary data

Supplementary data to this article can be found online at https://doi.org/10.1016/j.jmrt.2021.08.119.

REFERENCES

[1] Yap CY, Chua CK, Dong ZL, Liu ZH, Zhang DQ, Loh LE, et al. Review of selective laser melting: materials and applications. Appl Phys Rev 2015;2. https://doi.org/10.1063/1.4935926.

[2] Ma M, Wang Z, Zeng X. A comparison on metallurgical behaviors of 316L stainless steel by selective laser melting and laser cladding deposition. Mater Sci Eng A 2017;685:265–73. https://doi.org/10.1016/j.msea.2016.12.112.

[3] Murakami M, Yamada H, Maruyama T, Tanahashi H. Effects of alloying additions on Fe-Mn-Si shape memory alloys. ISIJ Int 1990;30:674–9. https://doi.org/10.2355/isijinternational.30.674.

[4] Chen J, Peng HB, Yang Q, Wang SL, Song F, Wen YH. Effect of carbon content on shape memory effect of Fe-Mn-Si-Cr-Ni-based alloys at different deformation temperatures. Mater Sci Eng A 2016;677:133–9. https://doi.org/10.1016/j.msea.2016.09.006.

[5] Kim D, Park C, Lee J, Hong K, Park Y, Lee W. Microstructure, shape memory behavior and mechanical properties of hot rolled Fe-17Mn-5Si-5Cr-4Ni-0.3C-1Ti shape memory alloy. Eng Struct 2021;239:112300. https://doi.org/10.1016/j.engstruct.2021.112300.

[6] Nishimura F, Watanabe N, Tanaka K. Transformation lines in an Fe-based shape memory alloy under tensile and compressive stress states. Mater Sci Eng A 1996;221:134–42. https://doi.org/10.1016/S0921-5093(96)10486-X.

[7] Rong LJ, Ping DH, Li YY, Shi CX. Improvement of shape memory effect in Fe-Mn-Si alloy by Cr and Ni addition. Scr Metall Mater 1995;32:1905–9. https://doi.org/10.1016/0956-716X(95)00049-2.

[8] Kajiwara S, Liu D, Kikuchi T, Shinya N. Remarkable improvement of shape memory effect in Fe-Mn-Si based shape memory alloys by producing NbC precipitates. Scr Mater 2001;44:2809–14. https://doi.org/10.1016/S1359-6462(01)00978-2.

[9] Dong Z, Klotz UE, Leinenbach C, Bergamini A, Czaderski C, Motavalli M. A novel Fe-Mn-Si shape memory alloy with improved shape recovery properties by VC precipitation. Adv Eng Mater 2009;11:40–4. https://doi.org/10.1002/adem.200800312.

[10] Leinenbach C, Arabi-Hashemi A, Lee WJ, Lis A, Sadegh-Ahmadi M, Van Petegem S, et al. Characterization of the deformation and phase transformation behavior of VC-free and VC-containing FeMnSi-based shape memory alloys by in situ neutron diffraction. Mater Sci Eng A 2017;703:314–23. https://doi.org/10.1016/j.msea.2017.07.077.

[11] Ferretto I, Kim D, Della Ventura NM, Shahverdi M, Lee W, Leinenbach C. Laser powder bed fusion of a Fe-Mn-Si shape memory alloy. Addit Manuf 2021;46:102071. https://doi.org/10.1016/j.addma.2021.102071.

[12] Lai MJ, Li YJ, Lillpopp L, Ponge D, Will S, Raabe D. On the origin of the improvement of shape memory effect by precipitating VC in Fe–Mn–Si-based shape memory alloys. Acta Mater 2018;155:222–35. https://doi.org/10.1016/j.actamat.2018.06.008.

[13] Lee WJ, Weber B, Feltrin G, Czaderski C, Motavalli M, Leinenbach C. Phase transformation behavior under uniaxial deformation of an Fe-Mn-Si-Cr-Ni-VC shape memory alloy. Mater Sci Eng A 2013;581:1–7. https://doi.org/10.1016/j.msea.2013.06.002.

[14] Alnajjar M, Christien F, Wolski K, Bosch C. Evidence of austenite by-passing in a stainless steel obtained from laser melting additive manufacturing. Addit Manuf 2019;25:187–95. https://doi.org/10.1016/j.addma.2018.11.004.

[15] Peng H, Wen Y, Liu G, Wang C, Li N. A Role of α martensite introduced by thermo-mechanical treatment in improving

shape memory effect of an Fe-Mn-Si-Cr-Ni alloy. Adv Eng Mater 2011;13:388—94. https://doi.org/10.1002/adem.201000282.

[16] Wen YH, Peng HB, Sun PP, Liu G, Li N. A novel training-free cast Fe-18Mn-5.5Si-9.5Cr-4Ni shape memory alloy with lathy delta ferrite. Scr Mater 2010;62:55—8. https://doi.org/10.1016/j.scriptamat.2009.10.004.

[17] Kim SH, Moon HK, Kang T, Lee CS. Dissolution kinetics of delta ferrite in AISI 304 stainless steel produced by strip casting process. Mater Sci Eng A 2003;356:390—8. https://doi.org/10.1016/S0921-5093(03)00152-7.

[18] Wegrzyn T. Delta ferrite in stainless steel weld metals. Weld Int 1992;6:690—4. https://doi.org/10.1080/09507119209548267.

[19] Kürnsteiner P, Wilms MB, Weisheit A, Barriobero-Vila P, Jägle EA, Raabe D. Massive nanoprecipitation in an Fe-19Ni-xAl maraging steel triggered by the intrinsic heat treatment during laser metal deposition. Acta Mater 2017;129:52—60. https://doi.org/10.1016/j.actamat.2017.02.069.

[20] Jägle EA, Choi PP, Van Humbeeck J, Raabe D. Precipitation and austenite reversion behavior of a maraging steel produced by selective laser melting. J Mater Res 2014;29:2072—9. https://doi.org/10.1557/jmr.2014.204.

[21] Günther J, Brenne F, Droste M, Wendler M, Volkova O, Biermann H, et al. Design of novel materials for additive manufacturing - isotropic microstructure and high defect tolerance. Sci Rep 2018;8:1—14. https://doi.org/10.1038/s41598-018-19376-0.

[22] Manvatkar V, De A, DebRoy T. Spatial variation of melt pool geometry, peak temperature and solidification parameters during laser assisted additive manufacturing process. Mater Sci Technol (United Kingdom) 2015;31:924—30. https://doi.org/10.1179/1743284714Y.0000000701.

[23] Mukherjee T, Wei HL, De A, DebRoy T. Heat and fluid flow in additive manufacturing — Part II: powder bed fusion of stainless steel, and titanium, nickel and aluminum base alloys. Comput Mater Sci 2018;150:369—80. https://doi.org/10.1016/j.commatsci.2018.04.027.

[24] Sun SH, Hagihara K, Nakano T. Effect of scanning strategy on texture formation in Ni-25 at.%Mo alloys fabricated by selective laser melting. Mater Des 2018;140:307—16. https://doi.org/10.1016/j.matdes.2017.11.060.

[25] Tari V, Rollett AD, Beladi H. Back calculation of parent austenite orientation using a clustering approach. J Appl Crystallogr 2013;46:210—5. https://doi.org/10.1107/S002188981204914X.

[26] Kajiwara S. Characteristic features of shape memory effect and related transformation behavior in Fe-based alloys. Mater Sci Eng A 1999;273:67—88. https://doi.org/10.1016/s0921-5093(99)00290-7. 275.

[27] Montoya-Coronado LA, Ruiz-Pinilla JG, Ribas C, Cladera A. Experimental study on shear strengthening of shear critical RC beams using iron-based shape memory alloy strips. Eng Struct 2019;200:109680. https://doi.org/10.1016/j.engstruct.2019.109680.

[28] Yasuda H, Nagira T, Yoshiya M, Sugiyama A, Nakatsuka N, Kiire M, et al. Massive transformation from δ phase to γ phase in Fe-C alloys and strain induced in solidifying shell. IOP Conf Ser Mater Sci Eng 2012;33. https://doi.org/10.1088/1757-899X/33/1/012036.

[29] Knutsson A, Hedström P, Odén M. Reverse martensitic transformation and resulting microstructure in a cold rolled metastable Austenitic stainless steel. Steel Res Int 2008;79:433—9. https://doi.org/10.1002/srin.200806149.